

Article

# Facile Synthesis, Characterization, and Adsorption Insights of Lanthanum Oxide Nanorods

Lakshmi Prasanna Lingamdinne , Janardhan Reddy Koduru \* , Yoon-Young Chang, Seon-Hong Kang and Jae-Kyu Yang \*

Department of Environmental Engineering, Kwangwoon University, Seoul 01897, Korea; swethasiri86@gmail.com (L.P.L.); yychang@kw.ac.kr (Y.-Y.C.); seonhong@kw.ac.kr (S.-H.K.)

\* Correspondence: reddyjchem@gmail.com (J.R.K.); jkyang@kw.ac.kr (J.-K.Y.); Tel.: +82-2-940-5496 (J.R.K.); +82-2-940-5769 (J.-K.Y.)

Received: 18 May 2020; Accepted: 22 July 2020; Published: 24 July 2020



**Abstract:** This study synthesized lanthanum oxide ( $\text{La}_2\text{O}_3$ ) nanorods to develop a practical approach for the removal of arsenic from groundwater.  $\text{La}_2\text{O}_3$  nanorods were synthesized by a simple hydrothermal process followed by calcination at  $500\text{ }^\circ\text{C}$  and were characterized by spectroscopic and microscopic techniques. To evaluate the adsorption mechanism of  $\text{La}_2\text{O}_3$  nanorods, adsorption parameters including solution pH, temperature, equilibrium isotherms, and kinetics for arsenic were studied. The results suggested that the arsenic uptake was a rate-limiting, monolayer adsorption interaction on the  $\text{La}_2\text{O}_3$  nanorods homogeneous surface. In addition, it was found that the adsorptive removal behavior of  $\text{La}_2\text{O}_3$  for As(V) was sensitive to the initial pH and temperature, and the maximum uptake amount of as prepared  $\text{La}_2\text{O}_3$  was found to be  $260.56\text{ mg/g}$  of As(V) at pH 6.0 and  $25\text{ }^\circ\text{C}$ . Furthermore, the uptake capacity of  $\text{La}_2\text{O}_3$  nanorods for As(V) increased with temperature. The resultant thermodynamic parameters ( $\Delta G^0$ ,  $\Delta H^0$ , and  $\Delta S^0$ ) suggested an endothermic adsorption of As(V) on  $\text{La}_2\text{O}_3$ . The adsorption capacity of  $\text{La}_2\text{O}_3$  was higher than that of several reported nanocomposites, suggesting its practical applicability and novelty for As-contaminated wastewater treatment.

**Keywords:** lanthanum oxide; nanorods; arsenic; adsorption; characterization; isotherm; thermodynamics

## 1. Introduction

Lanthanides are widely used in hydrogen storage, electrodes, gate insulators, adsorbents, and superconductors, owing to their versatility and multifunctionality [1–4]. In lanthanide series, lanthanum (La) is one of the lightest elements that has been widely used in various applications, including optoelectronic devices [5], phosphors [6], solid electrolytes [7], catalysts [8,9], sorbents [10], and gas sensors [11] in the form of oxide, carbonate, and phosphate. Currently, lanthanum oxide ( $\text{La}_2\text{O}_3$ ) is used in various applications, including water treatment [12,13], catalytic exhaust gas converters [14], and high-k gate dielectric materials [15]. Various methods have been adopted for the preparation of  $\text{La}_2\text{O}_3$  nanostructures, including precipitation, thermal decomposition, hydrothermal, sol gel, and pyrolysis methods [13,15–24]. The adsorption properties of  $\text{La}_2\text{O}_3$  mainly depend on its texture and surface morphology of materials. With this, there is still a research gap in developing a novel surface texture and morphology for  $\text{La}_2\text{O}_3$  in water treatment. Thus, this article focuses on the synthesis of nanostructured  $\text{La}_2\text{O}_3$  through simple precipitation followed by calcination at  $500\text{ }^\circ\text{C}$  and its adsorptive removal ability for As(V) in groundwater.

Arsenic is a highly toxic pollutant in the environment, occurring through natural and anthropogenic sources. Among existing arsenic forms in the environment, inorganic arsenic is more prevalent in +3 or

+5 oxidation states as arsenate ( $\text{H}_2\text{AsO}_4^-$ ,  $\text{HAsO}_4^{2-}$ ) or arsenite ( $\text{AsO}_3^{3-}$ ), respectively, under normal conditions of natural water [25,26]. The species  $\text{H}_2\text{AsO}_4^-$  and  $\text{HAsO}_4^{2-}$  are of great concern due to their high toxicity in natural water sources including drinking water [27]. Arsenic contamination of drinking water has been a global issue occurring in many countries including India, Bangladesh, Malaysia, Mexico, Hungary, New Zealand, USA, Spain, Japan, Canada, Taiwan, and Mainland China [27–29]. The exposure of arsenic for long-term periods may lead to lung, bladder, kidney, and skin cancer as well as changes in pigmentation [25,30]. The treatment of arsenic-contaminated wastewater is necessary. Some of researchers has been used lanthanum oxides for arsenic removal and those reported that the surface morphology, surface functions along with surface area and oxyanions are influence the adsorptive removal of lanthanum oxides [31,32]. Hence, we prepared lanthanum oxide with a specific morphology in this study.

Herein, we demonstrate a simple synthesis of  $\text{La}_2\text{O}_3$  nanorods 18 nm wide and approximately 160–200 nm long. The physical and chemical properties and purity of the obtained products were evaluated using advanced instrumental techniques including XRD, SEM, TEM, XPS, and FT-IR. Influencing parameters, including pH, kinetics, isotherms, and coexisting anions and cations, on the adsorptive removal of As(V) by  $\text{La}_2\text{O}_3$  were studied. Further, we carried out thermodynamic studies. The results suggest that the adsorptive removal of As(V) was an endothermic rate-limiting monolayer interaction on the homogeneous surface of  $\text{La}_2\text{O}_3$  nanorods. The maximum uptake of as prepared  $\text{La}_2\text{O}_3$  is 260.56 mg arsenic/g- $\text{La}_2\text{O}_3$  at 25 °C, and pH 6.0 was higher than that of several reported nanocomposites, suggesting its novelty and practical applicability for the treatment of As-contaminated water.

## 2. Materials and Methods

### 2.1. Materials

The materials used were of analytical reagent grade unless stated here. Junsei Chemicals Co., Ltd. (Tokyo, Japan) supplied the reagent  $\text{Na}_2\text{HAsO}_4 \cdot 7\text{H}_2\text{O}$ .  $\text{La}(\text{NO}_3)_3 \cdot 6\text{H}_2\text{O}$  was purchased from Daejung chemicals Co., Ltd. (Siheung-Si, Korea). Samchun Pure Chemicals Co., Ltd. (Pyeongtaek, Korea) supplied the reagents HCl and NaOH. HCl and NaOH were used to adjust the pH of the aqueous solutions.

### 2.2. Synthesis of $\text{La}_2\text{O}_3$ Nanorods

All chemicals were of analytical grade and used without further purification.  $\text{La}_2\text{O}_3$  was synthesized by simple hydrothermal precipitation followed by calcination.  $\text{La}(\text{NO}_3)_3 \cdot 6\text{H}_2\text{O}$  powder was dissolved in water and stirred vigorously to obtain a clear solution. The solution was adjusted to pH 10 using 5 M NaOH solution and stirred for 30 min and filtered. The obtained precipitate was then collected. The precipitate was evaporated to dryness at 100 °C and calcined at 500 °C for 4 h. The calcined products were stored and used for further studies. The calcination process was carried out at different time (1–6 h) intervals and different calcination temperatures (300, 400, 500, and 600 °C), but the morphology and surface area of the material remained the same at the above calcination at 500 °C for 4 h. Hence, the calcination condition 500 °C for 4 h was chosen as the optimum condition in the preparation of  $\text{La}_2\text{O}_3$  in this study.

### 2.3. Analytical Methods

A D/Max-2500 X-ray diffractometer (Rigaku, Tokyo, Japan) was used to evaluate the crystallinity and textural properties of the prepared adsorbents. The elemental composition was analyzed using a PHI Quantera-II XPS (Ulvac-PHI, Kanagawa, Japan). A scanning electron microscope (S-4300 and EDX-350, Hitachi, Tokyo, Japan) was used to investigate the surface morphology of the adsorbents. HR-TEM (JEM-4010, JEOL, Peabody, MA, USA) was used to measure the shape and particle size of the adsorbents. The samples for TEM were prepared by dispersing the final samples in distilled water,

and this dispersant was then dropped on carbon–copper grids covered by an amorphous carbon film. To prevent agglomeration of the adsorbent, the copper grid was placed on a filter paper at the bottom of a Petri dish. N<sub>2</sub> adsorption–desorption isotherms of the prepared materials were constructed using an Autosorb-1 (Quantachrome Instruments, Boynton Beach, FL, USA) instrument that was also used to measure the surface area, pore volume, and pore diameter. FT-Raman spectroscopy was carried out with BRUKER OPTICKGMBH and ESCALAB–210 (Barcelona, Spain) instruments. The pH at the potential of zero-point charge (pH<sub>zpc</sub>) of the sample was measured using the pH drift method. The pH of a solution of 0.01 M NaCl was adjusted between 2 and 12 by adding either HCl or NaOH. Adsorbent (0.1 g) was added to 50 mL of the solution. After the pH had stabilized (after 24 h), the final pH was recorded. The graph of the final pH vs. initial pH was used to determine the point at which the initial pH and final pH values were equal. This was taken as the pH<sub>zpc</sub> of the sample.

#### 2.4. Adsorption Process

As(V) stock solutions were freshly prepared by dissolving the desired amount of Na<sub>2</sub>HAsO<sub>4</sub>·7H<sub>2</sub>O (99% purity, Junsi, Japan). The required arsenic experimental solutions were prepared by diluting the stock solution. The batch studies were carried out using 0.1 g/L La<sub>2</sub>O<sub>3</sub> in a 50 mL Falcon tube contain metal ion solution (10 and 100 mg/L) at 25 °C and pH 6.0. The adsorption isotherms of As(V) on the adsorbent were studied at different temperatures (25, 35, and 50 °C) at pH 6.0 and a predetermined equilibrium time of 60 min. The solution pH influence on arsenic adsorption was estimated under pH ranges from 2.0 to 12.0 that were adapted using 0.1 M of HCl or NaOH solution under constant conditions. To evaluate the influence of associate ions on the adsorption efficiency of La<sub>2</sub>O<sub>3</sub> for As(V), NaCl, KCl, CaCl<sub>2</sub>, MgCl<sub>2</sub>, Na<sub>2</sub>SO<sub>4</sub>, Na<sub>3</sub>PO<sub>4</sub>, NaNO<sub>3</sub>, and NaHCO<sub>3</sub> salts were used to adapt the ionic concentration (0.05–0.5 mg/L), respectively. The adsorbed amount ( $q_e$ ) of As(V) was calculated using

$$q_e = (C_0 - C_e) \times V/m, \quad (1)$$

where the initial and equilibrium concentrations of As(V) (mg/L) are indicated by  $C_0$  and  $C_e$ , respectively,  $V$  is the aqueous phase volume (L), and  $m$  is the adsorbent weight (g). To increase the precision and accuracy of the data, duplicates, blanks, and reference standards were used in this study.

### 3. Results and Discussion

#### 3.1. Characterization

Figure 1a indicates the FT-IR spectra of the prepared nanomaterial. Figure 1a clearly shows a sharp band at 3576 cm<sup>-1</sup>, suggesting the O–H bond vibrates from the water molecules on the external surface of the material. The sharp bands at 1462 and 1318 cm<sup>-1</sup> were assigned to the asymmetric stretching mode of the CO<sub>3</sub><sup>2-</sup> group. It is highly probable that all CO<sub>3</sub><sup>2-</sup> groups occupy identical sites in the crystal lattice, so the lanthanum oxide precursor might be lanthanum carbonate due to the basic properties of La<sub>2</sub>O<sub>3</sub> which can further react with atmospheric CO<sub>2</sub> and water [33,34]. The sharp bands at 498, 672, 846, and 1050 cm<sup>-1</sup> were assigned to the stretching vibration of the La–O bond in La<sub>2</sub>O<sub>3</sub> [12,35]. The XRD pattern in Figure 1b shows the phases of La<sub>2</sub>O<sub>3</sub>. The 2θ values of 26.16°, 29.16°, 30.02°, 39.57°, 52.24°, and 55.53° denote La<sub>2</sub>O<sub>3</sub> [36]. The remaining diffraction peaks showed a small amount of La(OH)<sub>3</sub> in the La<sub>2</sub>O<sub>3</sub> product [23,36]. The crystallite size was calculated by Debye–Scherer’s formula,  $D = k\lambda / \beta \cos\theta$ , where  $D$  is the average crystalline size of the nanorod,  $\lambda$  is the wave length of radiation,  $\beta$  is the full width at a half maximum of the peak at 30.02°, and  $\theta$  is Bragg’s angle. The resultant mean crystalline size of the nanorods is 19.3 nm. The full-range XPS spectra of La<sub>2</sub>O<sub>3</sub> are displayed in Figure 1c, exhibiting the characteristic La and O1s peaks. The distinguished sharp peaks centered at 838.75 and 853.06 eV ascribed to La 3d<sub>5/2</sub> and 3d<sub>3/2</sub>, respectively, suggest La(III) [37]. Further, the high-resolution XPS of La 3d and O 1s (Figure 1d,e) confirmed the existence of La<sub>2</sub>O<sub>3</sub>. The La3d high-resolution XPS clearly showed that the bonding energy peaks at 832.68 and 849.84 eV are attributed to the corresponding two spin–orbits of 3d<sub>5/2</sub> and 3d<sub>3/2</sub> respectively, and the same is

also authenticated from the reported literature [38,39]. Further, the peaks at 836.32 and 853.57 eV can be attributed to the satellite peaks of the  $3d_{5/2}$  and  $3d_{3/2}$  spin-orbits, respectively [38], while the O 1s spectrum demonstrated a fine deconvolution with the two peaks. The peaks at 528.11 and 531.50 eV are designated to the oxygen anions from metallic oxygen (La–O) [37,38]. Further the SEM-EDX (Figure S1a) found La and oxygen along with traces of carbon from carbonate around 0.5  $k eV$  due to exposure to the natural atmosphere. These results confirmed the formation of  $La_2O_3$  with traces of carbonate at the surface, which is authenticated by the reported results [33,34]. Further, the SEM-EDX (Figure S1b) of  $La_2O_3$ , which was prepared under  $N_2$  atmosphere, is not shown with authentic carbon peaks, which are responsible for carbonate functions.

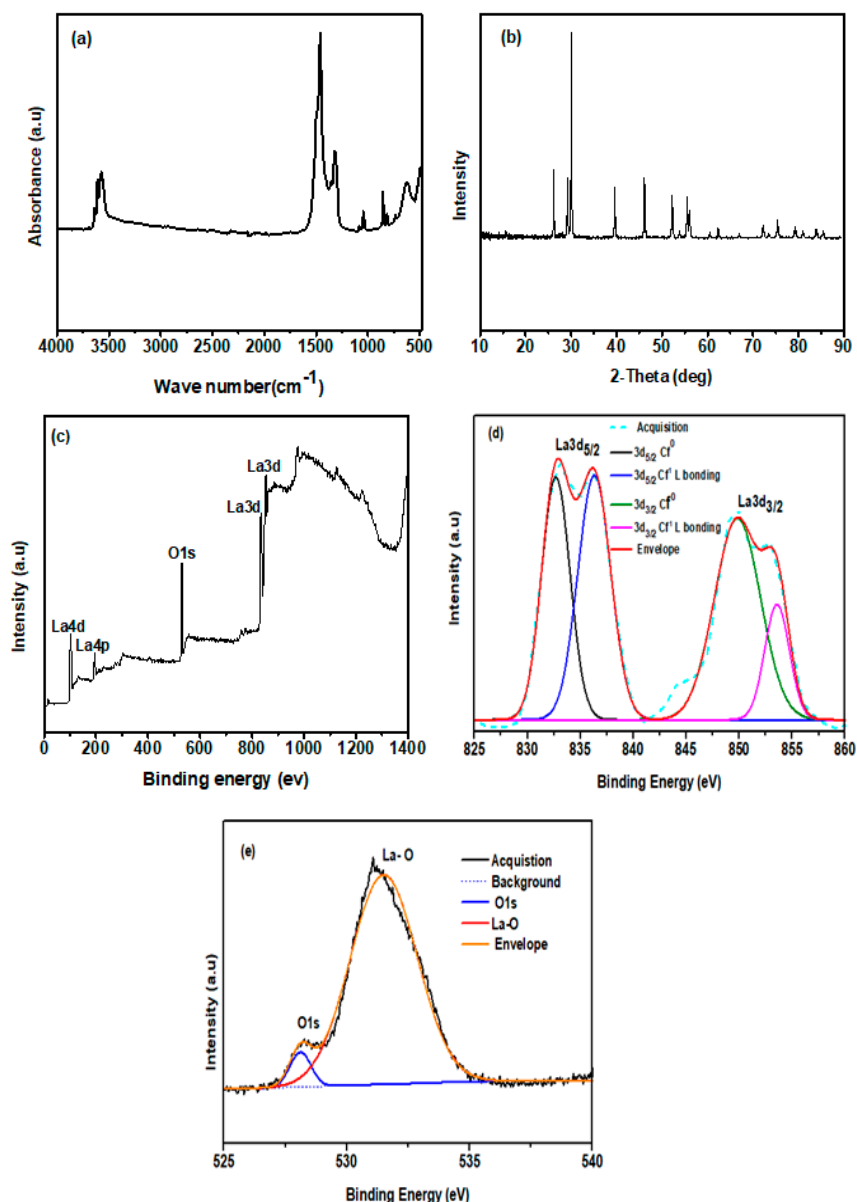


**Figure 1.** Spectroscopic characterization: (a) FT-IR spectra, (b) XRD patterns, and (c) XPS patterns of  $La_2O_3$  nanorods, and (d) high-resolution XPS of La 3d and (e) O 1s of prepared  $La_2O_3$ .

The morphologies of the  $La_2O_3$  samples were evaluated using SEM and TEM images. Figure 2 shows a typical SEM and TEM image of  $La_2O_3$  nanorods. The SEM images of the prepared compound confirmed the formation of nanoparticles. The nanorod texture from the TEM (Figure 2a) observations revealed rod-like nanostructures. The nanostructures of the synthesized  $La_2O_3$  exhibit uniform

morphology of the rods with a width of 18 nm and length of 160–200 nm. The resultant width of the prepared nanorod was close in agreement with Scherer's crystalline size. A Brunauer–Emmett–Teller (BET) measurement was conducted to find the pore volume, pore diameter, and surface area of the prepared  $\text{La}_2\text{O}_3$  nanorods. From the BET results, we found that the surface area of  $\text{La}_2\text{O}_3$  nanorods was  $18.76 \text{ m}^2/\text{g}$  with a pore volume of  $0.378 \text{ cm}^3/\text{g}$  and diameter of 1.785 nm. The overall microscopic results suggest that the prepared  $\text{La}_2\text{O}_3$  is classified as a nano-sized rod-shaped material.

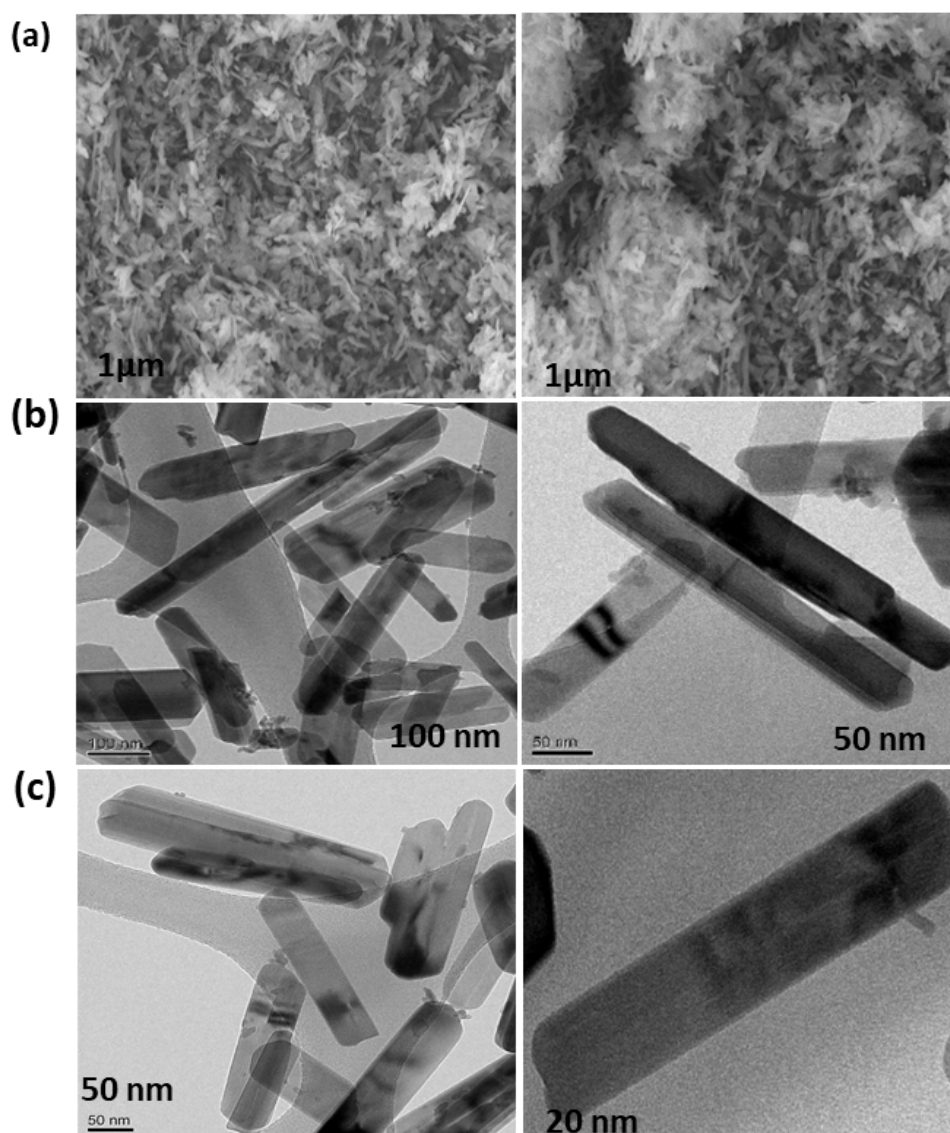


**Figure 2.** (a) SEM and (b,c) TEM images of  $\text{La}_2\text{O}_3$  produced by alkaline precipitation followed by calcination at  $500 \text{ }^\circ\text{C}$ .

### 3.2. Adsorption Studies

Figure 3a indicates the influence of the solution initial pH on the adsorptive removal of As(V) by the  $\text{La}_2\text{O}_3$  nanorods. The uptake of As(V) was rapidly increased from pH 2.0–3.0, reaching a plateau around 99.8% removal at pH 3.0–7.0. As pH is further increased (7.0–11.0), As(V) adsorptive removal slowly decreased. The slow increase in As(V) removal at pH 2.0–3.0 may be attributed to the predominance of As(V) in the molecular state of  $\text{H}_3\text{AsO}_4$  below pH 2.3 [40]. The maximum removal efficiency remained constant when As(v) pH increased to 3.0–7.0, possibly due to the more negatively charged As(V) species, leading to high adsorption on the positive surface of the  $\text{La}_2\text{O}_3$  nanorods

(pH < pHPZC (6.0) (Figure S2). A rapid decline emerged in the alkali pH 8.0–12.0 due to the presence of As(V) as  $\text{AsO}_4^{3-}$  in aqueous media, leading to electrostatic repulsion with the negative surface charge of the  $\text{La}_2\text{O}_3$  nanorods (pH > pHPZC (6.0)). However, there is significant adsorption removal under alkali conditions. Hence, the influence of the solution pH on As(V) adsorptive removal may be explained by two mechanisms: (1) electrostatic interaction and (2) surface complexation through ligand exchange [41]. As confirmed by FT-IR and XPS, there are active surface functional groups, lanthanum oxide, hydroxides, and traces of nitrate (Figure 1a) on the  $\text{La}_2\text{O}_3$  surface. At low pH solution (3.0–7.0),  $\text{La}_2\text{O}_3$  nanorods protonated the surface functions and formed positively charged surface functions that could adsorb negatively charged arsenic species ( $\text{H}_2\text{AsO}_4^-$  and  $\text{HAsO}_4^{2-}$ ) through electrostatic attraction and surface complexation [42]. At pH 8.0–11.0, the significant adsorption of As(V) may be due to the surface complexation of arsenic species through surface functional groups. However, the adsorption removal above pH > 10 was not significant. As shown in Figure 3b, the adsorptive removal of As(V) was efficient (99.30%) even at a low  $\text{La}_2\text{O}_3$  dosage (0.1 g/L). However, as the  $\text{La}_2\text{O}_3$  concentration increased from 0.1 to 1.0 g/L, the uptake capacity remained constant with an average removal efficiency of  $99.59 \pm 0.12\%$ .

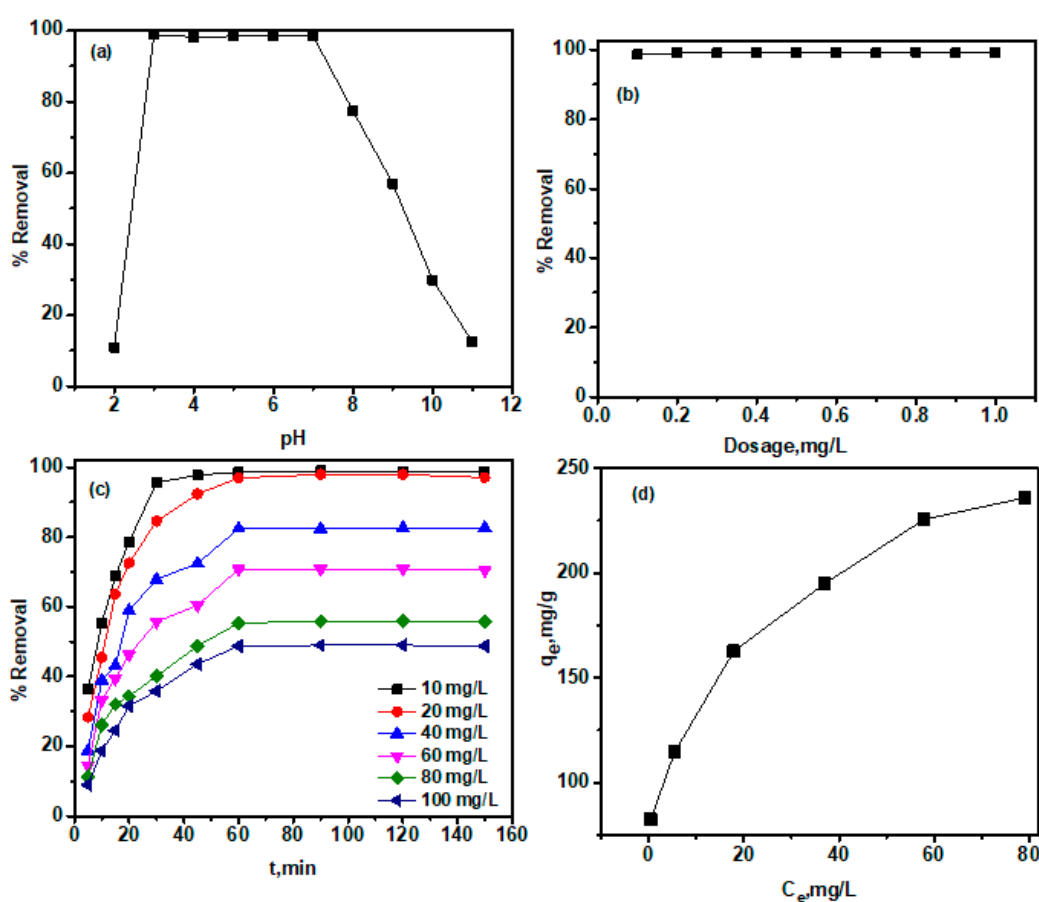


**Figure 3.** As(V) adsorption onto  $\text{La}_2\text{O}_3$  (10–100 mg/L, 0.1 g/L, pH 6.0) and the effects of (a) pH, (b) dosage (20 mg/L, pH 6.0) (c) kinetics, and (d) isotherms at 25 °C for 60 min equilibrium.

Adsorption kinetic studies were carried out to determine the removal of As(V) (10–100 mg/L) using the as-prepared  $\text{La}_2\text{O}_3$  nanorods (Figure 3b). The adsorptive removal of As(V) on  $\text{La}_2\text{O}_3$  increased rapidly as the contact time increased from 0–60 min. After 60 min, increasing the contact time caused the adsorption removal to remain constant. Pseudo first-order (PFO) (Equation (2)) and pseudo second-order (PSO) (Equation (3)) kinetics are used to investigate the adsorption kinetics of As(V) onto  $\text{La}_2\text{O}_3$ :

$$\text{PFO kinetic equation : } q = q_e \left( 1 - 10^{-k_1 \times t / 2.303} \right), \quad (2)$$

$$\text{PSO kinetic equation : } q = k_2 \times t \times q_e^2 / (1 + k_2 \times t \times q_e), \quad (3)$$

where the PFO and PSO rate constants are indicated by  $k_1$  and  $k_2$ , respectively. The resultant kinetic model fitting linear plots are shown in Figure S3.

The calculated parameters for the adsorption kinetics of As(V) onto La<sub>2</sub>O<sub>3</sub> nanorods at various metal concentrations (10–100 mg/L) are tabulated in Table 1. From the results, the PSO equation was found to be the best-fitting model considering their correlation coefficients  $R^2$  (PSO correlation coefficient) approximately equal to one. This was further confirmed by the close agreement of the theoretical  $q_e$  (mg/g) and predicted  $q_e$  (mg/g) of the PSO equation. Thus, the adsorption of As(V) on La<sub>2</sub>O<sub>3</sub> was a rate-limiting PSO reaction.

**Table 1.** La<sub>2</sub>O<sub>3</sub> nanorods adsorptive removal kinetics parameters for As(V) (10.0–100 mg/L) at pH 6.0, 25 °C for 60 min equilibrium time with 0.1 g/L nanorods.

Metal Concentration, mg/L	$q_e, Th,$ mg/g	PFO			PSO		
		$q_e, Cal,$ mg/g	$k_1$	$R^2$	$q_e, Cal,$ mg/g	$k_2$	$R^2$
10	86.98	34.57	0.0529	0.801	84.56	0.00215	0.999
20	118.98	88.97	0.0370	0.753	119.56	0.00049	0.999
40	145.68	116.97	0.0198	0.867	142.56	0.00027	0.998
60	185.69	135.69	0.0396	0.784	186.31	0.00018	0.995
80	205.69	158.95	0.0069	0.472	203.56	0.00021	0.991
100	245.68	185.98	0.0313	0.589	244.56	0.00044	0.992

Equilibrium adsorption isotherms are an important parameter for understanding adsorption mechanisms and describing the interaction between the adsorbate and adsorbent. An As(V) adsorption isotherm was obtained by varying the initial As(V) concentration (10–100 mg/L) (Figure 3d) and fitting the experimental data using Langmuir (Equation (4)), Freundlich (Equation (5)), and Temkin (Equation (6)) isotherm models to evaluate the adsorption process mechanism:

$$C_e/q_e = 1/q_m K_L + C_e/q_m, \quad (4)$$

$$\log q_e = \log K_F + n^{-1} \log C_e, \quad (5)$$

$$q_e = B \log K_T + B \log C_e \quad (6)$$

where the constants  $q_m$ ,  $K_L$  and  $n$ , and  $K_F$  are predicted from the intercept and slope of the plots of  $C_e/q_e$  vs.  $C_e$  (Equation (3)),  $\log C_e$  vs.  $\log q_e$  (Equation (4)), and  $q_e$  vs.  $\log C_e$  (Equation (5)) (Figure S4), respectively. These adsorption models represent the adsorption equilibrium at interfaces of the adsorbent with metal ions in a solution.

To determine the isotherm model most suitable in describing the As(V) adsorption process, data analysis was conducted using linear fitting isotherm models (Figure S3) and was considered based on the value of the correlation coefficients ( $R^2$ ) tabulated in Table 2.

**Table 2.** Isotherm predicted values for the adsorptive removal of As(V) on La<sub>2</sub>O<sub>3</sub> (0.1 g/L) nanorods at pH 6.0 and 25 °C for 60 min equilibrium.

Temperature, °C	Langmuir				Freundlich				Temkin			
	$q_{max},$ mg/g	$K_L$	$R^2$	$\chi^2$	$K_F,$ $mg/g \cdot (L/mg)^{1/n}$	$n$	$R^2$	$\chi^2$	$B$	$K_T$	$R$	$\chi^2$
25	260.56	1.88	0.995	2.16	185.05	5.30	0.945	9.87	98.60	127.96	0.971	13.45
35	285.98	2.56	0.999	1.65	135.08	6.88	0.917	12.69	99.88	212.93	0.948	18.97
50	305.69	3.12	0.998	1.98	131.05	4.06	0.963	20.76	56.87	306.12	0.909	17.89

Langmuir isotherms produced higher and more precise  $R^2$  values (close to 1) than the other tested isotherms. This was further confirmed from Pearson's chi-square ( $\chi^2$ ) analysis, which compared all isotherms on the same abscissa and ordinate to evaluate the best fitted model for the equilibrium adsorption isotherm data. The  $\chi^2$  is calculated using Equation (7)

$$\chi^2 = \sum \frac{(q_{exp} - q_{model})^2}{q_{model}} \quad (7)$$

where  $q_{model}$  and  $q_{exp}$  (mg/g) are the adsorption capacities determined from the model fitting and the experimental data, respectively. The  $\chi^2$  values for each model are shown in Table 2. From Table 2, it can be found that the resulting Pearson's chi-square ( $\chi^2$ ) errors have are lower for the Langmuir model fitting than others at three temperatures suggesting the Langmuir isotherm well explains the adsorption equilibrium data. Thus, the results of the isotherm suggest that monolayer adsorption occurred on  $\text{La}_2\text{O}_3$ 's energetically homogeneous surface. The maximum uptake capacity ( $q_e$ ) was found to be 260.56 mg/g at pH 6.0 and 25 °C. Further, the adsorption capacity of  $\text{La}_2\text{O}_3$ , prepared at  $\text{N}_2$  atmosphere, has been found to be 272.12 mg/g. This higher adsorption of  $\text{La}_2\text{O}_3$  (at  $\text{N}_2$  atmosphere) may be caused by the absence of carbonate on the  $\text{La}_2\text{O}_3$  surface (Figure S1b). Further, the adsorption capacity of  $\text{La}_2\text{O}_3$  nanorods for As(V) was comparable or more than the reported hybrid composites (Table 3), though there are similar reports offering comparable or lower As(V) removal efficiencies [25,40,42–45] as compared with the present material. Thus, these results prompted the potential of as prepared  $\text{La}_2\text{O}_3$  nanorods for arsenic-contaminated wastewater treatment.

**Table 3.** Comparison of As(V) adsorption capacities of various adsorbents.

Type of Adsorbent	$q_{max}$ (mg/g)	Conditions	Reference
		Initial Concentration, Dosage and pH	
Reduced graphene oxide-nickel ferrite (RGONF) nanocomposite	106.40	2–30 mg/L, 0.3 g/L and pH 6.5	[25]
Ce–Fe oxide decorated multiwalled carbon nanotubes	30.96	1–20 mg/L, 0.2 g/L and pH 4.0.	[40]
Sevelamer	133.00	0–250 mg/L, 1 g/L and pH 6	[42]
Core–shell structured Fe(0)@Fe oxide and Mn(0)@Mn oxide (ZVIM) nanocomposite	101.95	0.2–1.0 mg/L, 0.2 g/L and pH 6.5	[43]
Lanthanum-impregnated activated alumina	26.30	0–250 mg/L, 1.0 g/L and pH 7.0	[44]
Lanthanum-impregnated SBA-15	123.70	20–60 mg/L and pH 7.2	[45]
$\text{La}_2\text{O}_3$	260.56	10–100 mg/L, 0.1 g/L and pH 6.0	This work

### 3.3. Effects of Coexisting Ions

Real environmental water contains several ions that may influence the adsorptive removal of As(V). To assess the influence of competitive ions on As(V) adsorptive removal, 0.05–0.5 mg/L salt solutions of  $\text{K}^+$ ,  $\text{Na}^+$ ,  $\text{Mg}^{2+}$ ,  $\text{Ca}^{2+}$ ,  $\text{CO}_3^{2-}$ ,  $\text{SO}_4^{2-}$ ,  $\text{PO}_4^{3-}$ , and  $\text{NO}_3^-$  ions, respectively, were used and the results are shown in Figure 4. It was clearly observed from Figure 4, as salt concentration increased from 0.05 to 0.5 mg/L, that the adsorptive removal of As(V) decreased slightly from 99% to 90% and 83% with the respective cations,  $\text{Mg}^{2+}$  and  $\text{Ca}^{2+}$ . These results suggested that the tested cations were not significantly influenced by the adsorptive removal of As(V), where 7.7%, 92.7%, 39.5%, and 96.7% of the adsorptive removal of As(V) are shown in the presence of  $\text{CO}_3^{2-}$ ,  $\text{SO}_4^{2-}$ ,  $\text{PO}_4^{3-}$ , and  $\text{NO}_3^-$  anions, respectively. The adsorptive removal of As(V) on the adsorbent occurs between As(V) ions and  $\text{La}_2\text{O}_3$  ions at the adsorbent interface.  $\text{K}^+$  and  $\text{Na}^+$  exhibit a positive influence on the adsorption affinity of  $\text{La}_2\text{O}_3$  for As(V) than the other investigated cations and anions. However,  $\text{CO}_3^{2-}$  and  $\text{PO}_4^{3-}$  are significantly influenced by the adsorption affinity of  $\text{La}_2\text{O}_3$ . The significant effects of  $\text{CO}_3^{2-}$  on the adsorptive removal of arsenic might be due to an inner-sphere surface complexation [46]. That  $\text{PO}_4^{3-}$  decreased the adsorptive removal of As(V) significantly might be because As(V) and

$\text{PO}_4^{3-}$  are in the same symmetry (tetrahedral) and compete with each other for the surface sites at the nanocomposite surface [47,48]. Further, the results of the adsorption capacity of  $\text{La}_2\text{O}_3$ , prepared at  $\text{N}_2$  atmosphere, confirmed that the carbonate species predominately influence the adsorptive removal of As(V) (Figure S1b).

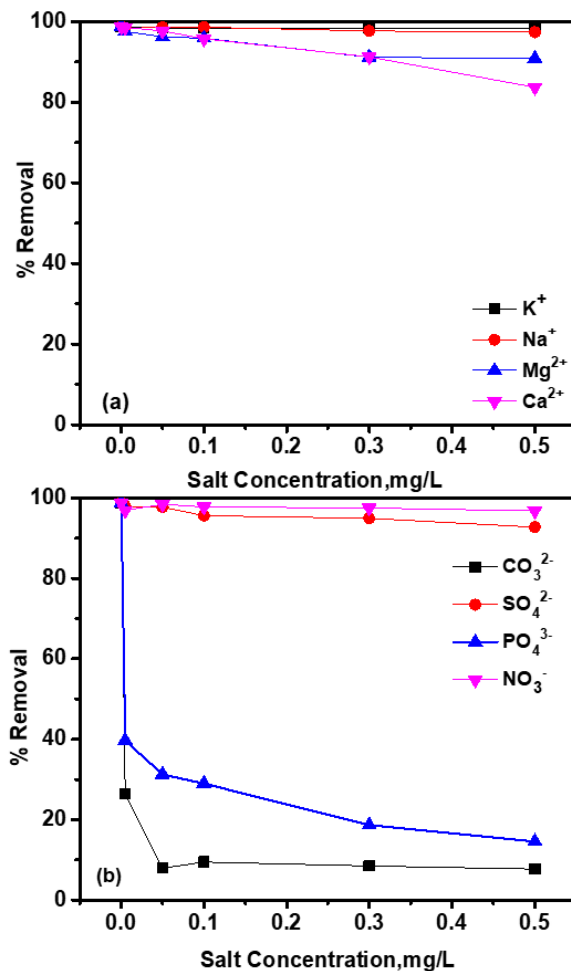


**Figure 4.** Co-existing ions: (a) cations' and (b) anions' influences on  $\text{La}_2\text{O}_3$  adsorptive removal of As(V) (10 mg/L) with 0.1 g/L  $\text{La}_2\text{O}_3$  dosage, at pH 6, and 25 °C for 60 min equilibrium.

### 3.4. Thermodynamic Parameters

The thermodynamic parameters, enthalpy ( $\Delta H^0$ ), entropy ( $\Delta S^0$ ), and Gibbs free energy ( $\Delta G^0$ ) of As(V) adsorption using  $\text{La}_2\text{O}_3$  can be calculated from  $RT \log K_C$  vs.  $T$  (Figure 5). The values of the free energy change ( $\Delta G^0$ ) are calculated using

$$\Delta G = -RT \ln K_C, \quad (8)$$

$$\Delta G = \Delta H - T\Delta S, \quad (9)$$

where the ideal gas constant is indicated by  $R$  in 8.314 kJ/mol, and temperature is indicated by  $T$  in "°C". Thus, the  $\Delta H^0$  and  $\Delta S^0$  can be measured from the slope and intercept of the  $RT \log K_C$  vs.  $T$  plot (Figure 5).

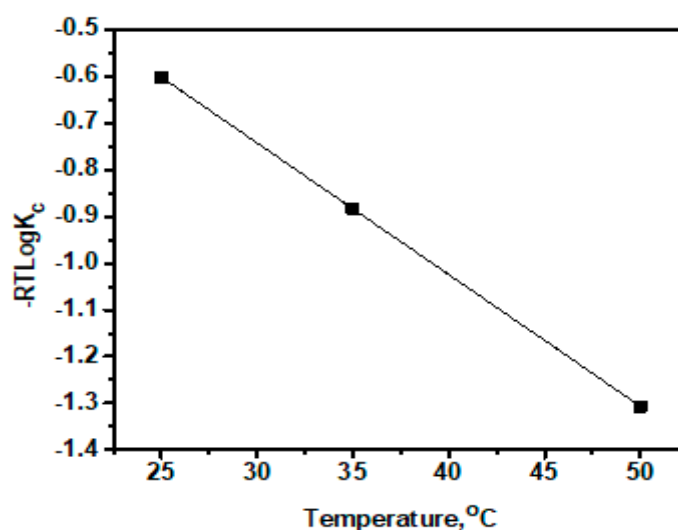


**Figure 5.** Temperature vs.  $\Delta G$  plot to understand the influence of temperature on the adsorption efficiency of  $\text{La}_2\text{O}_3$  (0.1 g/L) for As(V) (10 mg/L), at pH 6, and at 25 °C for 60 min equilibrium.

Based on Table 4, the negative  $\Delta G^0$  values suggest that the process of As(V) adsorptive removal by  $\text{La}_2\text{O}_3$  is spontaneous. The high  $\Delta G^0$  at 50 °C confers a favorable sorption at higher temperatures. The positive  $\Delta H^0$  suggests that the process of As(V) adsorptive removal by  $\text{La}_2\text{O}_3$  is endothermic. This is attributed to the assumption that the exothermic energy of the ions attached to the solid surface is lower than the endothermic energy of dehydration [49]. The positive value of  $\Delta S^0$  suggest increased randomness at the solid–liquid interface during the process of As(V) adsorptive removal by  $\text{La}_2\text{O}_3$ . Therefore, from the overall thermodynamic results, it is suggested that the uptake of As(V) on  $\text{La}_2\text{O}_3$  is an endothermic and spontaneous process.

**Table 4.** Thermodynamics for As(V) adsorption on  $\text{La}_2\text{O}_3$  (0.1 g/L) at pH 6.0.

Temperature, °C	$\Delta G^0$ (KJ/mol)	$\Delta H$ (KJ/mol)	$\Delta S$ (KJ/mol °C)	$\log K_c$
25	−601.291			2.892
35	−883.134	103.93	28.20	3.034
50	−1306.400			3.142

### 3.5. As(V) Adsorption Mechanism Using $\text{La}_2\text{O}_3$

Based on batch adsorption studies, including pH, kinetics, and equilibrium isotherms results, the adsorptive removal of As(V) with  $\text{La}_2\text{O}_3$  involves electrostatic interaction and surface complexation. From the pH experiment, high adsorption was obtained between pH 3.0–7.0, suggesting an electrostatic attraction between anionic arsenic species and the positive surface charge of the nanorods (Figure 6). However, arsenic removal decreased when pH was increased to 7.0–12.0, implying an electrostatic repulsion between the negative surface charge of the adsorbent and anionic species of As(V). Regardless, there is still significant adsorptive removal, revealing that the adsorption process involved chemical surface complexation predominantly at higher pH values (3.0–7.0). Thus, both electrostatic interaction and chemical surface complexation led to the adsorption process of As(V) at pH 3.0–7.0, which is further confirmed by FTIR results (Figure 7). Figure 7 clearly showed  $-\text{OH}$  ( $\sim 3576 \text{ cm}^{-1}$ ) and  $\text{La}-\text{O}$  ( $\sim 498 \text{ cm}^{-1}$ ) peaks altered by the adsorption of As(V), suggesting an adsorption process through surface complexation along with electrostatic interactions. The overall results of the adsorption process suggest that the electrostatic attraction of arsenic species through the protonated surface of  $\text{La}_2\text{O}_3$  and surface complexation are predominant in acidic conditions, while electrostatic repulsion and surface complexation of arsenic species with the  $\text{La}_2\text{O}_3$  surface are predominant in basic conditions. These representations are clearly shown in Figure 6 for better understanding.

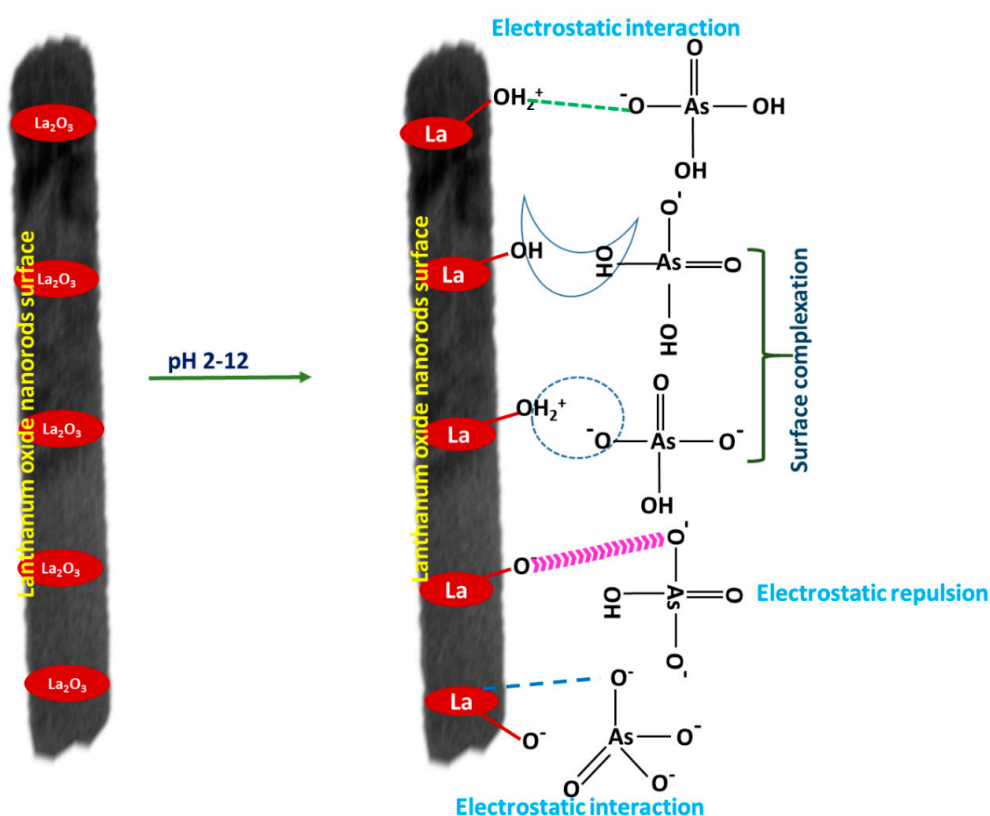


Figure 6. Adsorption mechanism of As(V) on La<sub>2</sub>O<sub>3</sub> nanorods at pH range 3.0–12.0.

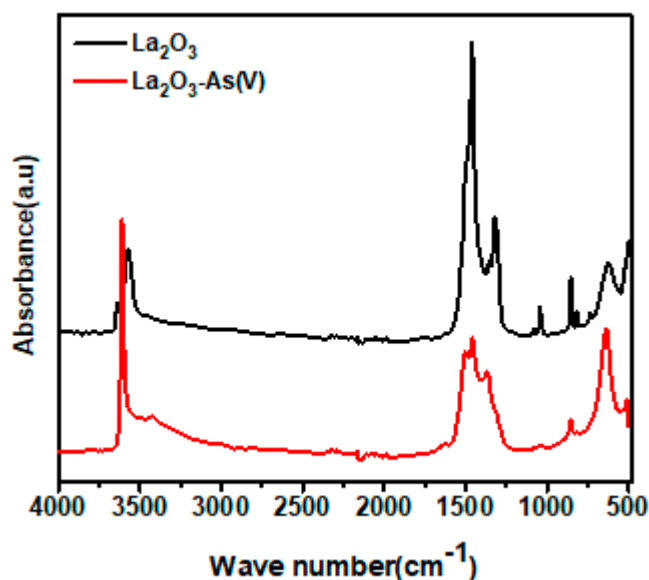


Figure 7. FT-IR spectra of La<sub>2</sub>O<sub>3</sub> nanorods before and after As(V) adsorption.

#### 4. Conclusions

La<sub>2</sub>O<sub>3</sub> was successfully synthesized to remove As(V) from contaminated water. The FT-IR image showed nanoparticles with an elemental composition of La and O as La<sub>2</sub>O<sub>3</sub>. Using TEM, the La<sub>2</sub>O<sub>3</sub> nanorod dimensions were measured, obtaining a width of 18 nm and length of 160–200 nm. The batch studies conferred that the adsorptive removal efficiency of La<sub>2</sub>O<sub>3</sub> nanorods for As(V) was sensitive to pH, temperature, and initial metal concentration. As(V) was most effectively removed at pH 3.0–7.0. The kinetic data were well explained by the PSO kinetics and the equilibrium isotherm data agreed with

the Langmuir isotherm model fitting. These results allow one to conclude that the uptake efficiency of  $\text{La}_2\text{O}_3$  for As(V) was rate-limiting kinetics with monolayer sorption on the homogeneous energetic surface of the nanorods. The maximum adsorptive removal capacity of  $\text{La}_2\text{O}_3$  has been found to be 260.56 mg/g at pH 6.0 and 25 °C, which is comparable with or more than the reported amounts of some hybrid materials. Therefore,  $\text{La}_2\text{O}_3$  is a potential material for As-contaminated wastewater treatment.

**Supplementary Materials:** The following are available online at <http://www.mdpi.com/2075-4701/10/8/1001/s1>, Figure S1. SEM-EDX spectrum of  $\text{La}_2\text{O}_3$  nanorods without  $\text{N}_2$  atmosphere (a) and of  $\text{La}_2\text{O}_3$  nanorods with  $\text{N}_2$  atmosphere (b). Figure S2. pH initial versus pH final graph and initial difference for pH pzc calculation for  $\text{La}_2\text{O}_3$ . Figure S3. PFO (a) and PSO (b) kinetics model linear fitting plots for As(V) adsorption on to  $\text{La}_2\text{O}_3$  nanorods. Metal initial concentration: 10 mg/L, Adsorbent dosage: 0.1 g/L, at pH 6, and 25 °C. Figure S4. Langmuir (a), Freundlich (b) and Temkin (c) isotherms on adsorptive removal of As(V) on to  $\text{La}_2\text{O}_3$  nanorods. Metal initial concentration: 10–100 mg/L, Adsorbent dosage: 0.1 g/L, at pH 6, and 25 °C for 60 min equilibrium.

**Author Contributions:** L.P.L. and J.R.K. conceived and designed the experiments; L.P.L. contributed to conducting experiments and contributed analysis tools; L.P.L., and J.R.K. analyzed the data and wrote the manuscript; J.-K.Y., S.-H.K., and Y.-Y.C. reviewed and edited the manuscript. All authors have read and agreed to the published version of the manuscript.

**Funding:** This research was funded by the National Research Foundation (NRF) of Korea, funded by the Ministry of Education (2019R111A1A01061487). The APC was funded by the Kwangwoon University, Seoul, Korea through Research Grant–2019.

**Acknowledgments:** This research was financially supported by the National Research Foundation (NRF) of Korea, funded by the Ministry of Education (2019R111A1A01061487) of the Korean Government. In addition, this study partially supported by the Kwangwoon University, Seoul, Korea through Research Grant–2019.

**Conflicts of Interest:** The authors declare no conflict of interest.

## References

1. Boldish, S.I.; White, W.B. Vibrational spectra of crystals with the A-type rare earth oxide structure.  $\text{La}_2\text{O}_3$  and  $\text{Nd}_2\text{O}_3$ . *Spectrochim. Acta Part A* **1979**, *35*, 1235. [[CrossRef](#)]
2. Goueron, J.; Michel, D.; Lejus, A.M.; Zarembowitch, J. Raman spectra of lanthanide sesquioxide single crystals: Correlation between A and B-type structures. *J. Solid State Chem.* **1981**, *38*, 288. [[CrossRef](#)]
3. Kang, S.W.; Rhee, S.W. Deposition of  $\text{La}_2\text{O}_3$  Films by Direct Liquid Injection Metallorganic Chemical Vapor Deposition. *J. Electrochem. Soc.* **2002**, *149*, 345. [[CrossRef](#)]
4. De Asha, A.M.; Critchley, J.T.S.; Nix, R.M. Molecular adsorption characteristics of lanthanum oxide surfaces: The interaction of water with oxide overlayers grown on Cu. *Surf. Sci.* **1998**, *405*, 201. [[CrossRef](#)]
5. Dakhel, A.A. Preparation and optical study of Au nanograins in amorphous La-oxide medium. *Colloids Surf. A Physicochem. Eng. Asp.* **2009**, *332*, 9–12. [[CrossRef](#)]
6. Ferhi, M.; Horchani-Naifer, K.; Férid, M. Hydrothermal synthesis and photoluminescence of the monophosphate  $\text{LaPO}_4:\text{Eu}(5\%)$ . *J. Lumin.* **2008**, *128*, 1777–1782. [[CrossRef](#)]
7. Imanaka, N.; Okamoto, K.; Adachi, G.Y. Water-insoluble lanthanum oxychloride-based solid electrolytes with ultra-high chloride ion conductivity. *Angew. Chem. Int. Ed.* **2002**, *41*, 3890–3892. [[CrossRef](#)]
8. Slagtern, Y.; Schuurman, C.; Leclercq, X.; Verykios, C. Mirodatos, Specific features concerning the mechanism of methane reforming by carbon dioxide over Ni/ $\text{La}_2\text{O}_3$  catalyst. *J. Catal.* **1997**, *172*, 118–126. [[CrossRef](#)]
9. Ordonez-Regil, E.; Drot, R.; Simoni, E.; Ehrhardt, J.J. Sorption of uranium (VI) onto lanthanum phosphate surfaces. *Langmuir* **2002**, *18*, 7977–7984. [[CrossRef](#)]
10. Tokunaga, S.; Wasay, S.A.; Park, S.W. Removal of arsenic (V) ion from aqueous solutions by lanthanum compounds. *Water Sci. Technol.* **1997**, *35*, 71–78. [[CrossRef](#)]
11. Imanaka, N.; Okamoto, K.; Adachi, N.G. A chlorine gas sensor based on the combination of  $\text{Mg}^{2+}$  cation conducting and  $\text{O}^{2-}$  anion conducting solid electrolytes with lanthanum oxychloride as an auxiliary electrode. *Electrochem. Commun.* **2001**, *3*, 49–51. [[CrossRef](#)]
12. Moothedan, M.; Sherly, K.B. Synthesis, characterization and sorption studies of nano lanthanum oxide. *J. Water Process Eng.* **2016**, *9*, 29–37. [[CrossRef](#)]
13. Yulin, L.; Jun, Y.; Xiaoci, L.; Huang, W.; Yu, T.; Zhang, Y. Combustion synthesis and stability of nanocrystalline  $\text{La}_2\text{O}_3$  via ethanalamine-nitrate process. *J. Rare Earths* **2012**, *30*, 48–52.

14. Keav, S.; Matam, S.K.; Ferri, D.; Weidenkaff, A. Structured perovskite-based catalysts and their application as three-way catalytic converters—A review. *Catalysis* **2014**, *4*, 226–255. [[CrossRef](#)]
15. Zhao, C.; Zhao, C.Z.; Werner, M.; Taylor, S.; Chalker, P. Dielectric relaxation of high-*k* oxides. *Nanoscale Res. Lett.* **2013**, *8*, 1–12. [[CrossRef](#)]
16. Tang, L.; Li, Y.M.; Xu, K.L.; Hou, X.D.; Lv, Y. Sensitive and selective acetone sensor based on its cataluminescence from nano-La<sub>2</sub>O<sub>3</sub> surface. *Sens. Actuators B* **2008**, *132*, 243. [[CrossRef](#)]
17. Cao, J.M.; Ji, H.M.; Liu, J.S.; Zheng, M.B.; Chang, X.; Ma, X.J.; Zhang, A.M.; Xu, Q.H. Controllable syntheses of hexagonal and lamellar mesostructured lanthanum oxide. *Mater. Lett.* **2005**, *59*, 408. [[CrossRef](#)]
18. Wang, S.Y.; Wang, W.; Qian, Y.T. Preparation of La<sub>2</sub>O<sub>3</sub> thin films by pulse ultrasonic spray pyrolysis method. *Thin Solid Films* **2000**, *372*, 50–53. [[CrossRef](#)]
19. Imanaka, N.; Masui, T.; Kato, Y. Preparation of the cubic-type La<sub>2</sub>O<sub>3</sub> phase by thermal decomposition of LaI<sub>3</sub>. *J. Solid State Chem.* **2005**, *178*, 395–398. [[CrossRef](#)]
20. Sheng, J.; Zhang, S.; Lv, S.; Sun, W.D. Surfactant-assisted synthesis and characterization of lanthanum oxide nanostructures. *J. Mater. Sci.* **2007**, *42*, 9565–9571. [[CrossRef](#)]
21. Wu, Q.Z.; Shen, Y.; Liao, J.F.; Li, Y.G. Synthesis and characterization of three-dimensionally ordered macroporous rare earth oxides. *Mater. Lett.* **2004**, *58*, 2688–2691. [[CrossRef](#)]
22. Hu, C.G.; Liu, H.; Dong, W.T.; Zhang, Y.Y.; Bao, G.; Lao, C.S.; Wang, Z.L. La(OH)<sub>3</sub> and La<sub>2</sub>O<sub>3</sub> nanobelts-synthesis and physical properties. *Adv. Mater.* **2007**, *19*, 470–474. [[CrossRef](#)]
23. Bazzi, R.; Flores-Gonzalez, M.A.; Louis, C.; Lebbou, K.; Dujardin, C.; Brenier, A.; Zhang, W.; Tillement, O.; Bernstein, E.; Perriat, P. Synthesis and luminescent properties of sub-5-nm lanthanide oxides nanoparticles. *J. Lumin.* **2003**, *102–103*, 445–450. [[CrossRef](#)]
24. Vadivel Murugan, A.; Navale, S.C.; Ravi, V. Synthesis of nano-crystalline La<sub>2</sub>O<sub>3</sub> powder at 100 °C. *Mater. Lett.* **2006**, *60*, 848–849. [[CrossRef](#)]
25. Lingamdinne, L.P.; Choi, Y.L.; Kim, I.S.; Chang, Y.Y.; Koduru, J.R.; Yang, J.K. Porous graphene oxide based inverse spinel nickel ferrite nanocomposites for the enhanced adsorption removal of arsenic. *RSC Adv.* **2016**, *6*, 73776–73789. [[CrossRef](#)]
26. Tuutijärvi, T.; Lu, J.; Sillanpää, M.; Chen, G. As (V) adsorption on maghemite nanoparticles. *J. Hazard. Mater.* **2009**, *66*, 1415–1420. [[CrossRef](#)] [[PubMed](#)]
27. Chen, S.L.; Dzung, S.R.; Yang, M.H.; Chiu, K.H.; Shieh, G.M.; Wai, C.M. Arsenic species in groundwaters of the black foot disease area, Taiwan. *Environ. Sci. Technol.* **1994**, *28*, 877–881. [[CrossRef](#)]
28. Karim, M. Arsenic in groundwater and health problems in Bangladesh. *Water Res.* **2000**, *34*, 304–310. [[CrossRef](#)]
29. Chakraborti, D.; Rahman, M.M.; Paul, K.; Chowdhury, U.K.; Sengupta, M.K.; Lodh, D.; Chanda, C.R.; Saha, K.C.; Mukherjee, S.C. Arsenic calamity in the Indian subcontinent. What lessons have been learned? *Talanta* **2002**, *58*, 3–22. [[CrossRef](#)]
30. Khosrow-pour, F.; Aghazadeh, M.; Sabour, B.; Dalvand, S. Large-scale synthesis of uniform lanthanum oxide nanowires *via* template-free deposition followed by heat-treatment. *Ceram. Int.* **2013**, *39*, 9491–9498. [[CrossRef](#)]
31. Misra, M.; Deba, C.N. Process for Removal of Selenium and Arsenic from Aqueous Streams. U.S. Patent 5,603,838, 18 February 1997.
32. Davis, S.A.; Misra, M. Transport model for the adsorption of oxyanions of selenium (IV) and arsenic (V) from water onto lanthanum-and aluminum-based oxides. *J. Colloid Interface Sci.* **1997**, *188*, 340–350. [[CrossRef](#)]
33. Karthikeyan, S.; Selvapandiyam, M. Effect of annealing temperature on the properties of lanthanum oxide (La<sub>2</sub>O<sub>3</sub>) nanoplates by reflux routes. *Int. J. Eng. Sci. Res. Technol.* **2018**, *7*, 559.
34. Mu, Q.; Wang, Y. Synthesis, characterization, shape-preserved transformation, and optical properties of La(OH)<sub>3</sub>, La<sub>2</sub>O<sub>2</sub>CO<sub>3</sub>, and La<sub>2</sub>O<sub>3</sub> nanorods. *J. Alloys Compd.* **2011**, *509*, 396–401. [[CrossRef](#)]
35. Xiao, Y.; Zongyu, F.; Xiaowei, H.; Li, H.; Zhiqi, L.; Qiang, W.; Yongke, H. Synthesis of lanthanum oxide nanosheets by a green carbonation process. *Chin. Sci. Bull.* **2014**, *59*, 1864–1867. [[CrossRef](#)]
36. Wang, K.; Wu, Y.; Li, H.; Li, M.; Guan, F.; Fan, H. A hybrid antioxidizing and antibacterial material based on Ag-La<sub>2</sub>O<sub>3</sub> nanocomposites. *J. Inorg. Biochem.* **2014**, *141*, 36–42. [[CrossRef](#)]
37. Hu, S.; Chi, B.; Pu, J.; Jian, L. Novel heterojunction photocatalysts based on lanthanum titanate nanosheets and indium oxide nanoparticles with enhanced photocatalytic hydrogen production activity. *J. Mater. Chem. A* **2014**, *2*, 19260–19267. [[CrossRef](#)]

38. Sanivarapu, S.R.; Lawrence, J.B.; Sreedhar, G. Role of surface oxygen vacancies and lanthanide contraction phenomenon of  $\text{Ln}(\text{OH})_3$  (Ln= La, Pr, and Nd) in sulfide-mediated photoelectrochemical water splitting. *ACS Omega* **2018**, *3*, 6267–6278. [[CrossRef](#)]
39. Sunding, M.F.; Hadidi, K.; Diplas, S.; Løvrvik, O.M.; Norby, T.E.; Gunnæs, A.E. XPS Characterization of In Situ Treated Lanthanum Oxide and Hydroxide Using Tailored Referencing and Peak Fitting Procedures. *J. Electron Spectrosc. Relat. Phenom.* **2011**, *184*, 399–409. [[CrossRef](#)]
40. Chen, B.; Zhu, Z.; Ma, J.; Qiu, Y.; Chen, J. Surfactant assisted Ce–Fe mixed oxide decorated multiwalled carbon nanotubes and their arsenic adsorption performance. *J. Mater. Chem. A* **2013**, *1*, 11355–11367. [[CrossRef](#)]
41. Sikder, M.T.; Tanaka, S.; Saito, T.; Kurasaki, M. Application of zero-valent iron impregnated chitosan-caboxymethyl  $\beta$ -cyclodextrin composite beads as arsenic sorbent. *J. Environ. Chem. Eng.* **2014**, *2*, 370–376. [[CrossRef](#)]
42. Kyzas, G.Z.; Siafaka, P.I.; Kostoglou, M.; Bikiaris, D.N. Adsorption of As(III) and As(V) onto colloidal microparticles of commercial cross-linked polyallylamine (sevelamer) from single and binary ion solutions. *J. Colloid Interface Sci.* **2016**, *474*, 137–145. [[CrossRef](#)] [[PubMed](#)]
43. Panda, A.P.; Rout, P.; Sanjukta, A.K.; Jha, U.; Swain, S.K. Enhanced performance of a core–shell structured Fe@Fe oxide and Mn@Mn oxide (ZVIM) nanocomposite towards remediation of arsenic contaminated drinking water. *J. Mater. Chem. A* **2020**, *8*, 4318–4333. [[CrossRef](#)]
44. Shi, Q.; Yan, L.; Chan, T.; Jing, C. Arsenic adsorption on lanthanum-impregnated activated alumina: Spectroscopic and DFT study. *ACS Appl. Mater. Interfaces* **2015**, *7*, 26735–26741. [[CrossRef](#)] [[PubMed](#)]
45. Jang, M.; Park, J.K.; Shin, E.W. Lanthanum functionalized highly ordered mesoporous media: Implications of arsenate removal. *Microporous Mesoporous Mater.* **2004**, *75*, 159–168. [[CrossRef](#)]
46. Wang, C.; Luo, H.; Zhang, Z.; Wu, Y.; Zhang, J.; Chen, S. Removal of As (III) and As (V) from aqueous solutions using nanoscale zero valent iron-reduced graphite oxide modified composites. *J. Hazard. Mater.* **2014**, *268*, 124–131. [[CrossRef](#)]
47. Yu, F.; Sun, S.; Ma, J.; Han, S. Enhanced removal performance of arsenate and arsenite by magnetic graphene oxide with high iron oxide loading. *Phys. Chem. Chem. Phys.* **2015**, *17*, 4388–4397. [[CrossRef](#)]
48. Sigdel, A.; Park, J.W.; Kwak, H.; Park, P.K. Arsenic removal from aqueous solutions by adsorption onto hydrous iron oxide-impregnated alginate beads. *J. Ind. Eng. Chem.* **2016**, *35*, 277–286. [[CrossRef](#)]
49. Huang, J.Y.; Wu, Z.W.; Chen, L.W.; Sun, Y.B. The sorption of Cd (II) and U (VI) on sepiolite: A combined experimental and modeling studies. *J. Mol. Liq.* **2015**, *209*, 706–712. [[CrossRef](#)]



© 2020 by the authors. Licensee MDPI, Basel, Switzerland. This article is an open access article distributed under the terms and conditions of the Creative Commons Attribution (CC BY) license (<http://creativecommons.org/licenses/by/4.0/>).